

# Accurate Detection of Doppler Cardiograms With a Parameterized Respiratory Filter Technique Using a K-Band Radar Sensor

Shuqin Dong<sup>✉</sup>, Graduate Student Member, IEEE, Yuchen Li<sup>✉</sup>, Graduate Student Member, IEEE, Jingyun Lu<sup>✉</sup>, Graduate Student Member, IEEE, Zhi Zhang, Changzhan Gu<sup>✉</sup>, Senior Member, IEEE, and Junfa Mao<sup>✉</sup>, Fellow, IEEE

**Abstract**—Cardiogram is one of the most important factors for health assessment. As a new expression of cardiograms, the Doppler cardiograms (DCGs) detected remotely via Doppler radar sensor (DRS) provide rich details of the heart motion. However, the existing techniques for measurement of DCG requires that the subject holds his/her breath to avoid the disturbance caused by respiration. To realize the accurate detection of DCGs in the presence of respiration, a high-linearity *K*-band dc-coupled continuous-wave (CW) DRS with digital dc-tuning function was custom-designed and a novel parameterized respiratory filter (PRF) algorithm was proposed to precisely remove the respiratory signal. Both simulation and experimental results show that the proposed PRF algorithm has better DCG extraction performance than the conventional methods. Furthermore, the experimental results in normal and clinical environments show that the grained differential DCG (D-DCG) has promising potential in professional heart rate variability (HRV) analysis and heart diseases diagnosis, which means the proposed DCGs detection has the potential to be a convenient, comfortable, and reliable way for daily and clinical heart health assessment.

**Index Terms**—Differential Doppler cardiogram (DCG), Doppler cardiogram (DCG), Doppler radar sensor (DRS), heart diseases, parameterized respiratory filter (PRF).

## I. INTRODUCTION

IN RECENT years, noninvasive health monitoring has been one of the most popular research topics in the microwave community [1]. Heart is the most important organ of human body. Heart health monitoring is gradually becoming a daily need for more and more people [2]. It is also a must routine

Manuscript received 14 March 2022; revised 3 May 2022; accepted 23 May 2022. Date of publication 24 June 2022; date of current version 13 January 2023. This work was supported in part by the National Key Research and Development Program of China under Grant 2019YFB2204604, in part by the National Science Foundation of China under Grant 62171277, and in part by the Shanghai Municipal Science and Technology Major Project under Grant 2021SHZDZX0102. This article is an expanded version from the IEEE Radio & Wireless Week, Las Vegas, Nevada USA, January 16–19, 2022 [DOI: 10.1109/RWS53089.2022.9719905]. (Corresponding author: Changzhan Gu.)

Shuqin Dong, Yuchen Li, Jingyun Lu, Changzhan Gu, and Junfa Mao are with the MoE Key Laboratory of High-Speed Electronic Systems and the MoE Key Laboratory of Artificial Intelligence, Shanghai Jiao Tong University, Shanghai 200240, China (e-mail: changzhan@sjtu.edu.cn).

Zhi Zhang is with Shanghai General Hospital, Shanghai 201613, China.

Color versions of one or more figures in this article are available at <https://doi.org/10.1109/TMTT.2022.3184019>.

Digital Object Identifier 10.1109/TMTT.2022.3184019

for patients in inpatient and clinical scenarios. Electrocardiogram (ECG) is the widest used approach to obtain the cardio information among these scenes [3]. However, the contact electrodes required by ECG measurements make it unsuitable for long-term daily heart monitoring [4], [11].

The detection of heart activities based on radar technique has been investigated for decades [5], such as the apexcardiograms [6], heart sounds [7], and cardiac timings [10]. However, the cardiac information they can provide is limited and suffers from the accuracy problem. The recent study on near-field self-injection-locked radar and the super-regenerative oscillator (SRO) radar showed accurate peripheral pulse waveform detection performance, which can be used for cuffless blood pressure monitor and plethysmograph detection [8], [9]. However, it requires contact measurement. Also, the detailed heart activity information it provides is indirect and unclear now.

Recently, the “Doppler cardiogram” (DCG) has been proposed, which can be remotely measured by Doppler radar. It describes the combined atrial and ventricular motions conducted to the skin [11]. All the timing information of the P-wave, QRS complex, and the T-wave in ECGs can be derived from fine-grained DCG waveforms with high accuracy, which can be used to calculate the reliable cardiac timings like R-R intervals [11]. Moreover, in physiology, DCG actually reflects human heart’s mechanical activities in terms of velocity and acceleration information that cardiac motions “project” on the skin, which can directly provide the relevant motion information of the cardiac contractions and relaxations of chambers in heart [11]. This means DCGs might provide diagnostic information for heart diseases with abnormal mechanical activities such as atrial fibrillation (AF) and premature heartbeat (PHB).

During the measurement of human DCG in the long-term health monitoring scenarios, the inevitable presence of respiration makes it difficult to detect the accurate DCG signal. The previous research [11] detects the pure DCG waveform when the subject holds his/her breath, while the state-of-the-art research [12] applies digital low-pass finite impulse response (FIR) filter with a fixed cutoff frequency of 0.8 Hz to the linearly recovered chest-wall motion to extract or subtract out the respiration signal. However, the distortion

caused by respiration still exists, and it impacts the accuracy of DCG detection. Accurate DCG detection in the presence of respiration is still challengeable.

In the past, the heartbeat waveform is usually modeled as sinusoidal [16], [19]. However, the actual DCG is not such an ideal signal with narrowband in spectrum. Every cycle of DCG has many dents and small peaks which means the DCG signal has many significant harmonics generating a large signal band. To avoid the nonlinear distortion to the DCG signal, the high-linearity radar sensor and linear signal demodulation is important to detect the accurate DCG.

The most common way to separate cardiac and respiratory components is filtering. While the real-life respiration waveform typically has many harmonics [12], [14], which would interfere with reliable detection of the much smaller DCG signals. The higher harmonics of respiration could reside within DCG bandwidth. This overlap in spectrum makes it impossible to completely reduce the influence of respiration by a simple high-pass/low-pass/bandpass filter. The RELAX-based methods proposed in [15] and [16] can sequentially estimate and remove the respiration harmonics to obtain accurate heart rate in frequency domain. However, the accurate waveform extraction in the time-domain is out of consideration. Other methods aiming to measure the heart activity based on radar are mainly focusing on the direct estimation of heart rate and heart rate variability (HRV) analysis [17], such as wavelet-based [18] and match-filter-based method [19].

In this work, which is an expanded version of [20], an improved 24-GHz continuous-wave (CW) Doppler radar system radar system with dc-coupled baseband circuit was custom-designed. The simulation experiment was carried out before practical experiments, and the results indicate that the designed system achieved a high linearity to obtain the accurate target motion. Besides, a novel parameterized respiration filter (PRF) algorithm is proposed to retrieve the DCGs waveform from mixed signal in the presence of respiration. The detailed derivation and simulated results show the proposed algorithm can precisely recover DCG, especially in the cases that respiration harmonics appear in the DCG bandwidth. The comparisons with the commonly used signal separation methods in the state-of-the-art literatures [20]–[22] are also conducted in this article. The result shows the proposed algorithm has best DCG extraction performance with quite low computation cost. Then, extensive practical experiments in both normal office environment and clinical environment have been carried out. The experimental results demonstrated that the DCGs obtained by the proposed technique were aligned well with ECG waveform, and the R-R intervals obtained by differential DCG (D-DCG) exhibited high accuracy both in the short-term (10 s) and long-term experiments (10 min). It even showed enhanced accuracy than that in breath-hold condition of healthy people [11], [12], which provides reliable data for HRV analysis [24]. Furthermore, the D-DCG waveforms of patients with heart diseases (AF and PHB) obtained in this work exhibited similar disease symptom characteristics compared to ECGs. These results show promising potentials in applying DCGs in wide applications such as home healthcare,

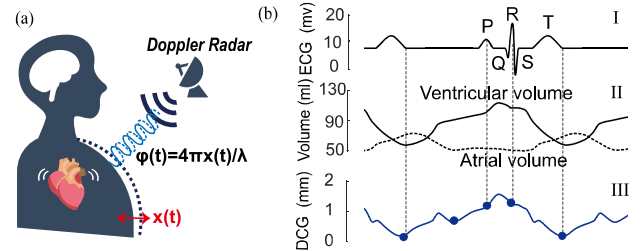


Fig. 1. (a) Scenario of CW Doppler radar vital sign detection and (b) the corresponding ECG, heart chambers' volume change and DCG which were replicated based on MRI data reported in [11].

sleep monitoring, clinical heart monitoring, and heart disease auxiliary diagnosis.

## II. METHOD

### A. DCG Detection Based on Radar

The CW Doppler radar sensor (DRS) detects displacement by measuring the phase change  $\varphi(t)$  modulated on the waves reflected from the moving target, as shown in Fig. 1(a). The mixer outputs  $I(t)$  and  $Q(t)$  in a typical quadrature radar system can be expressed as follows:

$$I(t) = A_I \cdot \cos[4\pi x(t)/\lambda + \varphi_0 + \Delta\varphi] + DC_I \quad (1)$$

$$Q(t) = A_Q \cdot \sin[4\pi x(t)/\lambda + \varphi_0 + \Delta\varphi] + DC_Q \quad (2)$$

where  $A_I$  and  $A_Q$  are the amplitudes of the quadrature  $I/Q$  signals, respectively,  $DC_I/DC_Q$  are the dc offsets,  $\varphi_0$  is the initial phase of the radar system,  $x(t)$  is the target motion,  $\lambda$  is the wavelength of the radar carrier, and  $\Delta\varphi$  is the residual phase noise.

Aiming to linearly recover the target motion  $x(t)$  with no distortion, (1)/(2) have to be calibrated to remove the dc offsets by fitting the  $I/Q$  signals on the unit circle [11], [25]. Then the motion  $x(t)$  can be linearly reconstructed by applying modified differentiate and cross-multiply (MDACM) algorithm [25].

During the detection of human vital signs, since the continuous wave transmitted by the  $K$ -band radar can hardly penetrate in human body, the radar signal mainly carries the displacement information of human chest wall as shown in Fig. 1(a). In stable settings, human would not have much large-scale random body movement like lying on the bed, the detected motion  $x(t)$  thus mainly contains human cardiac and respiration components.

In physiology, human cardiac motion is caused by the heart mechanical activities, e.g., contraction and diastole, which can be scientifically quantified by heart chambers' volume change via magnetic resonance imaging (MRI) or echocardiographic [28]. According to the correspondence between heart chambers' volume change and ECG whose waveforms were replicated in panels I and II of Fig. 1(b), these values are changing coordinately in time-domain [27]. The corresponding chest-wall motion  $D(t)$  caused by heart chambers' time-variant volume change based on the heart model [26] was plotted in panel III of Fig. 1(b). This motion can be detected by DRS and was named as "DCG" in [11]. Therefore, during

the DCG detection in presence of human normal respiration, the chest-wall motion  $x(t)$  can be modeled as

$$x(t) = x_r(t) + D(t) \quad (3)$$

where  $x_r(t)$  is the chest-wall motion caused by human breathing.

Obviously, if there is a method which can efficiently remove the respiration motion  $x_r(t)$ , the DCG waveform  $D(t)$  can be accurately recovered.

### B. Respiratory Profiling

In the state-of-the-art related works [16], [19], the respiration waveform is modeled as being sinusoidal. However, the sinusoidal model does not match with the real-life situation well. Lots of practical data showed that respiration is a motion that has very low frequency and contains a short period of stationary moment after the lung deflation which also has many significant harmonics [13], [14]. Besides, different people have different respiration waveforms. A prototype respiration pulse proposed in [14] fits well to the empirical observations

$$x_r(t) = \sin^p \pi f_R t, \quad 0 \leq t \leq \frac{1}{f_R} \quad (4)$$

where  $f_R$  is respiration frequency, and  $p$  is a scalar parameter defining the waveform type.

To establish the correlation between the parameter of respiration model and actual respiration waveform, a new respiration model is proposed in this article

$$x_r(t) = \cos^{2n} \pi f_R t, \quad n \in Z^+. \quad (5)$$

According to Euler's formula, (5) can be rewritten as

$$x_r(t) = \left( \frac{e^{i\pi f_R t} + e^{-i\pi f_R t}}{2} \right)^{2n}. \quad (6)$$

After the binomial expansion

$$\begin{aligned} x_r(t) &= \frac{1}{2^{2n}} \sum_{k=0}^{2n} C_n^k (e^{i\pi f_R t})^{2(n-k)} \\ &= \frac{1}{2^{2n}} \sum_{k=0}^n C_n^k \cos[2(n-k)\pi f_R t] \\ &= \frac{1}{2^{2n-1}} \left[ \cos 2n\pi f_R t + C_{2n}^1 \cos 2(n-1)\pi f_R t \right. \\ &\quad \left. + C_{2n}^2 \cos 2(n-2)\pi f_R t + \dots + \frac{C_{2n}^n}{2} \right]. \quad (7) \end{aligned}$$

It can be concluded that the parameter  $n$  in (5) is the number of respiratory frequency components in spectra including fundamental frequency and  $(n - 1)$  harmonics. Fig. 2(a)–(c) shows the waveforms of respiration when  $n$  is in different values. Fig. 2(d)–(f) show the corresponding Fourier transform spectrums. It can be seen that the parameter  $n$  controls how many harmonics would appear in spectrum, and the larger  $n$  would result in a narrower pulse. In practice, the waveform of  $n = 1$  is usually corresponding with the breath with equal time of inhale and exhale, the waveforms of  $n = 3$  and

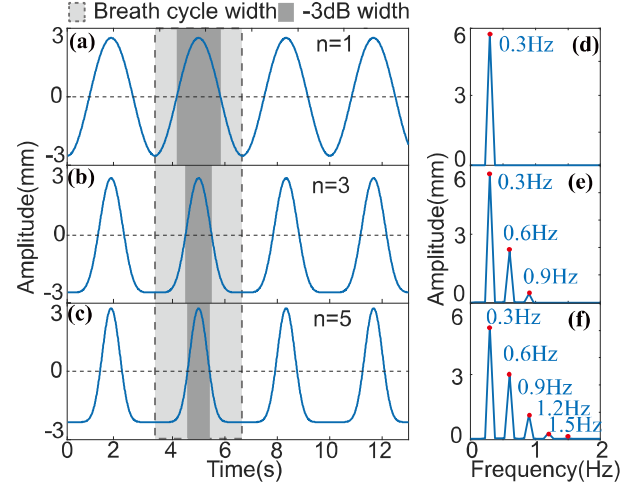


Fig. 2. (a)–(c) Three respiration waveforms with different respiratory parameter  $n$ . (d)–(f) The corresponding FT spectrums of simulated waveforms showed in (a)–(c).

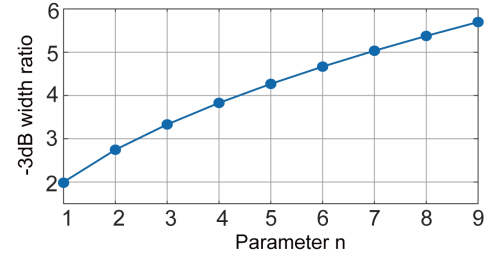


Fig. 3. Curve of  $r_{-3\text{dB}}$  over  $n$ .

$n = 5$  are corresponding with the different levels of exhale time extension. All this waveform is common in real life according to the respiratory dataset in [29]. To establish the relationship between the waveform and parameter  $n$ , this article proposed a waveform parameter  $-3$  dB width ratio  $r_{-3\text{dB}}$ , which is calculated by

$$r_{-3\text{dB}} = \frac{1}{\Delta t_{-3\text{dB}} \cdot f_R} \quad (8)$$

where  $\Delta t_{-3\text{dB}}$  is the time length of the narrow pulse waveform width which is identified in dark gray zone in Fig. 2(a)–(c). The  $r_{-3\text{dB}}$  also refers to the ratio of light and dark gray zones' widths in Fig. 2.

In radar detection scene, the heart and respiration motion are mixed in the original radar demodulated signal as presented in (3). The respiration component would maintain the original feature at the respiratory maximum speed point, which is located at half the peak of the mixed waveform. So, the time intervals for calculating  $\Delta t_{-3\text{dB}}$  in formula (8) are selected at half the peak of the respiratory waveform.

Fig. 3 shows the curve of  $r_{-3\text{dB}}$  over  $n$ . It can be seen that there is a correlation between these two parameters. Moreover, this correlation can be mathematically represented as a formula.

First, the  $-3$  dB width ratio  $r_{-3\text{dB}}$  has a mathematically analytical solution

$$r_{-3\text{dB}} = \frac{\pi}{2 \arccos \left( 0.5^{\frac{1}{2n}} \right)}. \quad (9)$$

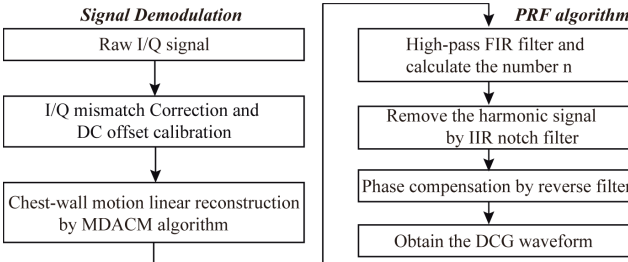


Fig. 4. Flowchart of the proposed DCG extraction method.

Then, we can derive the parameter  $r_{-3\text{ dB}}$  from waveform, and then the number of harmonics  $n$  can be estimated by

$$n = \frac{1}{2 \log_{\frac{1}{2}} \left[ \cos \left( \frac{\pi}{2r_{-3\text{ dB}}} \right) \right]}. \quad (10)$$

#### C. Parameterized Respiration Filter (PRF) Algorithm

To obtain the accurate DCG signal, the respiration harmonics should be removed as much as possible. Based on the respiration model demonstrated in Section II-B, a PRF algorithm is proposed in this article. After signal demodulation, the PRF algorithm would operate on the highly recovered chest-wall motion to extract DCG in the presence of respiration. Fig. 4 shows the flowchart of proposed DCG extraction method.

First, since the amplitude of respiration is much larger than that of heartbeat in practice, the breath frequency  $f_R$  can be easily estimated from frequency spectrum of  $x(t)$  in (3). Then the time length  $\Delta t_{-3\text{ dB}}$  can be calculated in every cycle of breath. The  $-3$  dB bandwidth ratio  $r_{-3\text{ dB}}$  can be calculated by (8). Then from (10), the number of breathing harmonics can be obtained.

Second, to effectively remove these frequency components of respiration, a FIR high-pass filter with narrow transition bandwidth and  $(n - 1)$  infinite impulse response (IIR) filters with narrow  $-3$  dB bandwidth are designed. The FIR high-pass filter aims to remove the dc and low-frequency component, and is designed to have a 0.1-Hz transition bandwidth with 0.7-Hz cutoff frequency. Due to the narrow transition band between cardiac and respiratory components, such transition bandwidth of the filter is necessary for signal separation. On the other hand, the IIR notch filters aims to remove the harmonics, and are designed to have a 0.002-Hz  $-3$  dB bandwidth and an 80-dB stopband attenuation with central frequencies at  $nf_R$ . Similarly, narrowband is designed to minimize the impact on DCG in-band features. Such IIR notch filters require a high-order design, which means more running time of the algorithm. Considering the tradeoff between the efficiency of the algorithm and the effectiveness of the filter, 6th order is selected.

It is generally known that IIR filter will introduce phase distortion and make the signal waveform anamorphic. We performed phase compensation method to recover the waveform of extracted DCG. The detailed process is shown in Table I. According to the theory of zero-phase digital filer [23], the output signal  $y(n)$  has precisely zero phase distortion and

TABLE I

PROCESS OF PHASE COMPENSATION

Input	The discrete signal $x(n)$ after IIR notch filter
Output	The phase compensated signal $y(n)$
<b>Process:</b>	
Step 1	Reverse the signal $x(n)$ and get $x_r(n)$ , $x_r(n) = x(N-1-n)$
Step 2	Filter the signal $x_r(n)$ with designed IIR notch filter
Step 3	Reverse the filtered signal from step 2, and get the output signal $y(n)$

$N$  is the data length of input signal  $x(n)$ .

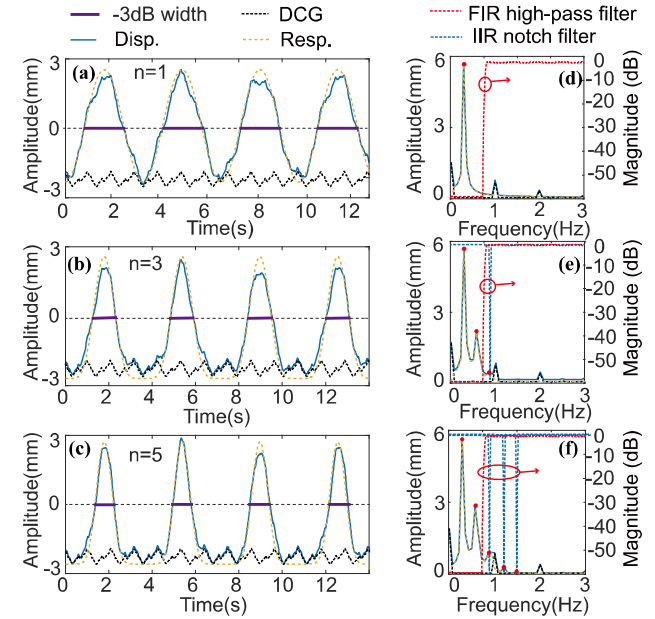


Fig. 5. (a)–(c) The simulation waveforms of respiration, DCG and mixed signal in the case of  $n = 1, 3, 5$ , respectively. (d)–(f) The corresponding FT spectrums of simulated waveforms as shown in (a)–(c), and the magnitude response of used filters in PRF algorithm.

magnitude modified by the square of the designed IIR filter's magnitude response. The process will therefore compensate the waveform distortion induced by IIR filter's non-linear phase response.

To verify the effectiveness of the PRF algorithm, we numerically simulated 10-s chest-wall motion with different respiration waveforms as shown in Fig. 5. In the simulation, the DCG signal is mimicked according to the waveform in panel III of Fig. 1(b) which has a 1-Hz heartbeat frequency and 0.4-mm amplitude. The respiratory signal was generated by the proposed mathematical model (5) with an amplitude of 5 mm. And from (3), the simulated chest-wall motion can be generated. Gaussian noises were simultaneously added to the simulation with 40-dB SNR.

Fig. 5(a)–(c) shows the simulated waveforms of respiration, DCG and chest-wall motion in the cases of  $n = 1, 3, 5$ , respectively. The lengths of the thick purple lines indicate the  $\Delta t_{-3\text{ dB}}$  in (8). Fig. 5(d)–(f) shows the corresponding frequency spectrums of simulated waveforms in Fig. 5(a)–(c), and the magnitude response of the used filters in PRF algorithm. Obviously, in the case of  $n = 1$ , the respiration signal only has a fundamental frequency component with no harmonics, so a high-pass FIR filter with 0.7-Hz cut-off frequency can remove the respiration. Whereas, in the cases of  $n = 3$  and

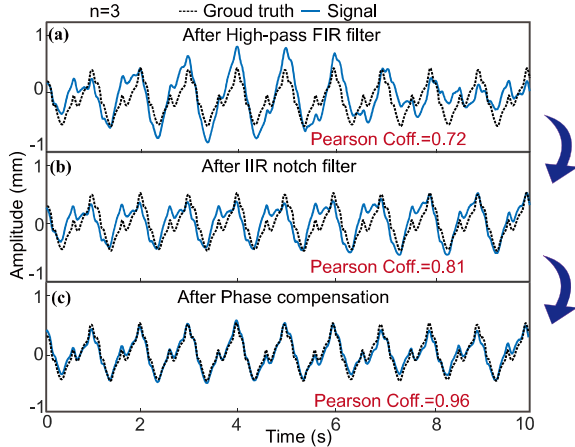


Fig. 6. (a)–(c) Results after each step of the PRF algorithm in the case of parameter  $n = 3$ .

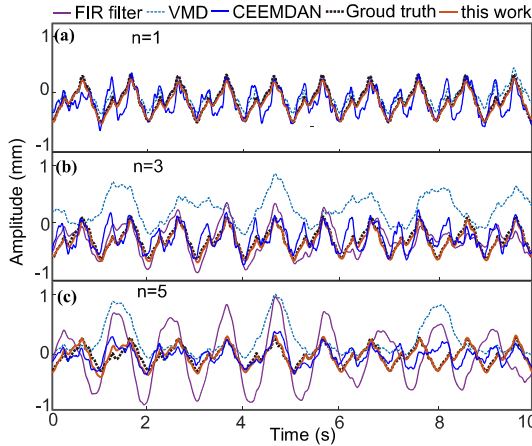


Fig. 7. Comparison of the DCG extraction performance among the FIR filter method, VMD, CEEMDAN and the PRF algorithm proposed in this work for different simulated respiratory waveform with different parameter  $n$ . (a)–(c) Comparison results in the case of  $n = 1, 3, 5$ , respectively.

$n = 5$ , the respiration signals have two harmonics and four harmonics, respectively. In this situation, the IIR notch filters should be employed, for harmonics greater than 3-order have frequencies greater than 0.9 Hz that are within the band of DCG.

To further elaborate on the performance of the PRF algorithm, the results after each step of the algorithm in the case of parameter  $n = 3$  is illustrated in Fig. 6. It can be seen that the signal after high-pass filter has a lot of distortion due to the remaining respiratory frequency components that overlap with DCG band. After the IIR notch filter step, the periodicity of the DCG signal is restored but the characteristic waveform is still distorted. Finally, after the phase compensation, it can be seen that the extracted DCG signal fits well with the ground truth with the Pearson correlation coefficient of 0.96, which implies that almost all the details of DCG were preserved.

Fig. 7 shows the comparison of the performance under different signal separation algorithms, e.g., variational modal decomposition (VMD) method [21], complete ensemble empirical mode decomposition (CEEMDAN) method [22], and simple high-pass FIR filter [12]. It can be seen that the FIR filter method and PRF algorithm show the similar

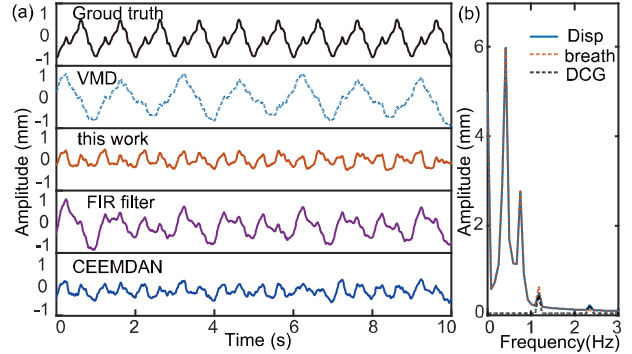


Fig. 8. Results of signal extraction algorithms when respiration harmonic coincides with the frequency of heart rate. (a) The waveform in time domain. (b) The spectrum of simulated respiratory signal, DCG signal and mixed signal.

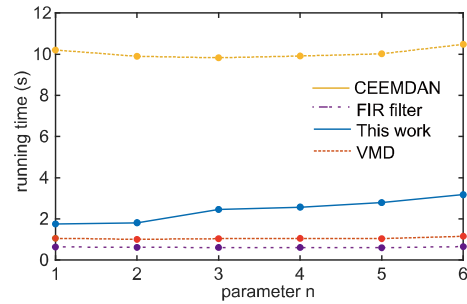


Fig. 9. Comparison of the running time of the DCG extraction methods when handling 10-s signals with different respiratory parameter  $n$ .

performance and obtain accurate DCG with respect to ground truth when respiration has no harmonics, i.e.,  $n = 1$ . However, the CEEMDAN and VMD show the large distortion compared with ground truth, especially the CEEMDAN. In the cases of respiration with harmonics falling into the DCG band, e.g.,  $n = 3, 5$  in Fig. 7(b) and (c), the PRF algorithm can still handle this situation while the other methods show large distortion. It should be noted that in practice it is very common for respiratory signals to contain higher harmonics, so this feature of algorithm is important for DCG detection in the presence of respiration.

In addition, we also got the simulation results from the different algorithms when a respiration harmonic coincides with the frequency of heart rate exactly, like the breath frequency  $f_R$  is 0.4 Hz, the heart rate is 1.2 Hz and the breath signal has 3rd order harmonic. However, all the above algorithms show large distortion, as shown in Fig. 8. The result of PRF algorithm seems to keep a little periodicity, but the features of DCG are all lost. This is because the part of the DCG component has been filtered out by notch filter. In practical application, the breath rate and heart rate are all slowly changing and this extreme case will not last long though.

The comparison of computational efficiency between different algorithms was conducted in this part. As shown in Fig. 9, the FIR filter method and VMD algorithm show the least running time due to the low complexity. However, these two methods suffer from the severe distortion in the cases when respiratory harmonics falling into the DCG band.

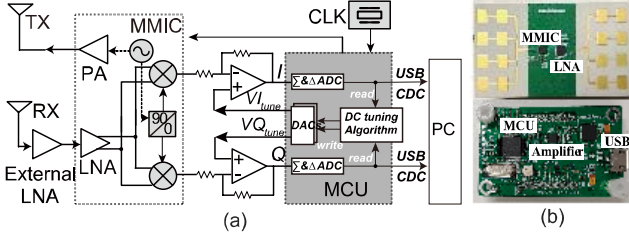


Fig. 10. (a) System block diagram of the 24-GHz radar sensor. (b) The implementation of 24-GHz radar sensor.

The CEEMDAN algorithm shows the maximum running time which is much longer than the other methods. The running time of PRF algorithm will slightly increase when the number of respiratory harmonics increases. This is because the more notch filters are used of the process.

### III. MEASUREMENT

#### A. Measurement Setup

Fig. 10(a) shows the detailed block diagram of the DRS developed for measuring the DCG based on a 24-GHz front-end silicon germanium millimeter-wave integrated circuit (MMIC). An additional K-band low noise amplifier (LNA) is employed to improve the noise performance of the radar receiver. The I/Q signals sampled by the embedded 16-bit sigma-delta analog-to-digital convertors (SDADCs) inside the microcontroller unit (MCU) can be transmitted to a computer with full-speed USB interface.

Fig. 10(b) shows the implemented board-integrated radar sensor. The substrate used is Rogers 4350B, whose dielectric constant and the loss tangent are 3.48 and 0.0037, respectively. To avoid signal distortion in the digital baseband domain and precisely measure the complete characteristic details of target motion which is important for DCG detection, the receiver leverages an adaptive dc tuning strategy running in the MCU as a feedback loop. As shown in Fig. 10(a), the adaptive dc tuning technique makes it possible to make full use of the dynamic range of the ADCs with low hardware complexity.

#### B. Performance Measurement Experiment

To verify the linearity of radar system and signal demodulation process during DCG detection in the presence of respiration, a simulation experiment was implemented in this part. A motor stage from Zaber Technologies with a fixed metal plate was employed to generate the chest-wall motions of different respiratory parameter  $n$  for simulation as shown in Fig. 5(a)–(c). This computer-controlled, motorized linear stage has a 1-μm position accuracy which is suited for providing such a high lifetime motion. Experimental setup is exhibited in Fig. 11(a). The metal plate is placed at the radial direction of radar with the distance of 50 cm.

In the experiment, we generated three kinds of respiration waveform with  $n = 1, 3, 5$ , respectively, in the simulation experiment. Fig. 11(b) shows the raw I/Q signals detected for 15-s simulation experiment in the case of  $n = 3$ , along with the fitting circle. The experimental results are shown in Fig. 12. In Fig. 12(a)–(c), the recovered motions plotted in

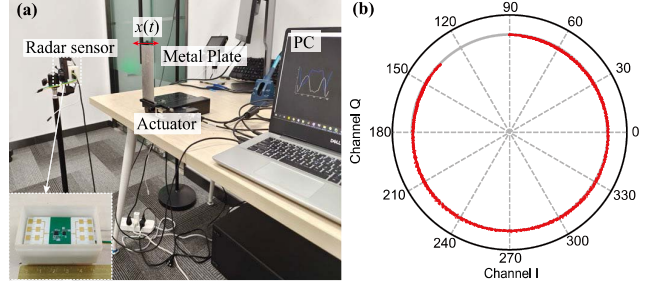


Fig. 11. (a) Experimental setup of simulated chest-wall motion sensing with the implemented 24 GHz radar sensor. The insert shows the photograph of radar sensor. (b) The I/Q trajectory of simulation experiment in the case of  $n = 3$ .

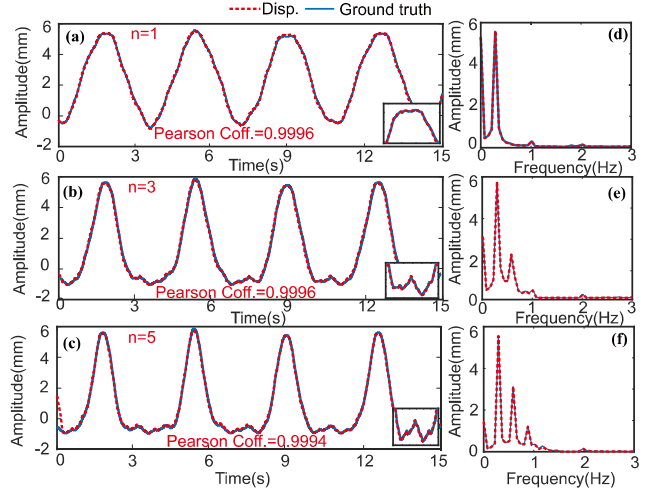


Fig. 12. Experimental results of chest-wall motion simulated with metal plate. (a)–(c) The original waveforms and recovered motions when respiratory parameter  $n = 1, 3, 5$ . The insert figures are zoom-in segments showing the low-speed respiratory motions. (d)–(f) The corresponding FT spectra of the waveforms in (a)–(c).

red dashed line are obtained by the linear phase demodulation algorithm, and the ground truth plotted in black line is the stage's movement. It can be seen that the recovered motions fit well with the ground truth. The insert figures are zoom-in segments showing the low-speed respiratory motions, where the DCG characteristics disappear but the recovered motion also fits well. The recovered motions of different parameter  $n$  are with a Pearson correlation coefficient of 0.9996, 0.9996, 0.9994, respectively, compared to the ground truth. And the corresponding frequency spectra in Fig. 12(d)–(f) also show little distortion with respect to ground truth.

#### C. DCG Measurement Experiments in Different Scenarios

The practical experiments in three different scenarios were carried out to validate the accuracy of DCG measurement, namely subject in normal environment with sitting posture, subject in normal environment with supine posture, and patient in clinical environment, as shown in Fig. 13(a)–(c), respectively.

First, as shown in Fig. 13(a), during the experiment of subject in normal environment with sitting posture, the subject who is 24-year-old male weighed 65 kg and 176 cm tall was sitting still leaning on the back of a chair. The radar sensor was fixed on the fixation frame and placed around 40 cm away

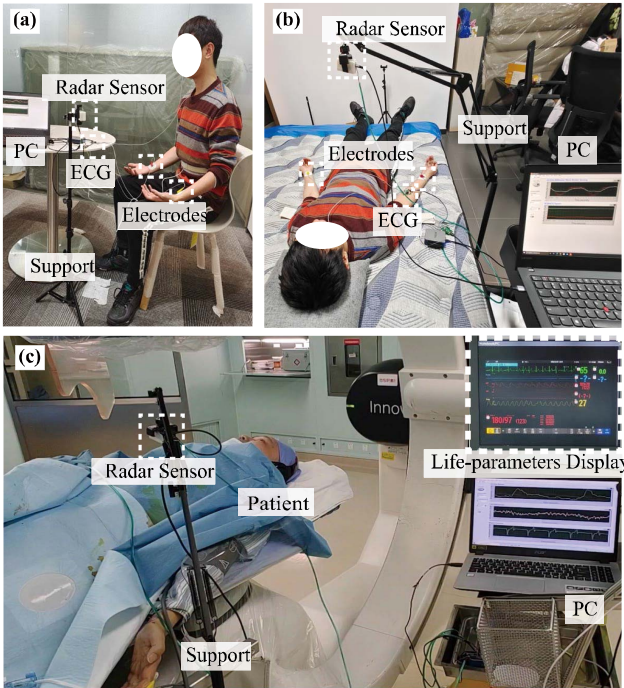


Fig. 13. Experimental setups: DCG measurement experiment in normal environment (a) with sitting posture, (b) with supine posture, and (c) in clinical environment. Inset shows the life-parameters monitor display in OT.

from the subject. The short time (12 s) experimental results are shown in Fig. 14(a) and (b).

Second, the normal experiment with supine posture of the same subject was conducted on the bed. The radar sensor was also fixed on the fixation frame and placed around 40 cm away from the subject' chest as shown in Fig. 13(b). The short time (12 s) experimental results are shown in Fig. 14(c) and (d).

In these measurements, the subject was breathing normally and an integrated single-end ECG sensor based on AD8232 was simultaneously used to detect the ECG using electrodes placed on his wrists and chest for comparison purpose. The output analog signal of the ECG sensor and the radar baseband signal can be synchronously sampled by USB-6001 (DAQ @ National Instruments) which allows an accurate comparison of the correspondence between ECG and extracted DCG. It is noted that the synchronous measurement on analog signals in DAQ shares a synchronous sampling clock and starts at the same time through programing in LabVIEW. It means this synchronous data sampling system has higher reliability than the Bluetooth platform in [11].

In Fig. 14(a) and (c), the signal waveforms from the experimental data in different scenarios are plotted. The panels I and IV of these figures show ECG signals detected ECG signals and the demodulated displacement signal with MDACM algorithm [25] from the  $I/Q$  signals detected by DRS, and Fig. 14(b) and (d) shows the corresponding spectra of the signal in Panel IV. Panel II shows the DCG waveforms extracted by PRF algorithm and HPF, and Panel III shows the D-DCG waveform. In Panel IV, the parameter  $\Delta t_{-3\text{dB}}$  in PRF algorithm can be measured from the demodulated signal waveform. Then according to the spectrum of displacement

signal, the fundamental frequency of respiration  $f_R$  can be easily found. Afterward, the respiratory parameter  $n$  can be obtained by (8) and (10). It can be seen that the calculated parameter  $n$  is a reliable indicator of the number of respiratory frequency components according to the corresponding spectrum in Fig. 14(b) and (d). And the extracted DCG waveform by the PRF algorithm shows good correspondence with the ECG signal.

To locate the characteristic points of DCG which corresponding to P wave, QRS wave, and T wave of ECG signal, we did differential process to the DCG waveform and get the velocity curve named D-DCG in this work. Based on the synchronized experimental data from DRS and ECG device, we found that there is a good temporal correspondence between the minimum point of D-DCGs named "B" and the QRS wave of the ECG which are also easy to be positioned automatically by Findpeaks algorithm in MATLAB [28]. Besides, the first valley before point B in D-DCG waveform named "A" corresponds to the beginning of P wave, and the first peak after the point B named "C" corresponds to the ending of T wave. These points were marked on the D-DCG waveform as shown in Fig. 14.

Sequentially, the clinical experiment was conducted at the bedside in a hybrid operation theater (OT) of Shanghai General Hospital, as shown in Fig. 13(c). A patient multi-parameters life monitor, Philips MP2 M8102A, was used for patient in this OT. This monitor can simultaneously record the ECG and other life parameters. The patients with coronary heart disease (CHD) had just finished the angiography operation and is in the postoperative observation period, at which time the life-parameters monitoring was still working. The ECG and radar signal recording were simultaneously made for comparison purpose while the patient is in supine position with normal breath. The written informed consent was obtained from the patient. The experimental results of a regular patient and a patient with persistent AF are shown in Fig. 15.

For the regular patient, the 12-s experimental results are shown in Fig. 15(a) and (b). The D-DCG waveform from the DCG obtained by proposed technique in Panel III of Fig. 15(a) shows different waveform features, the first valley after point B is much larger compared to the DCG results of healthy people in Fig. 15(a) and (c). However, this did not affect the positioning of point A-C.

The experiment on the persistent AF patient was also performed in the hospital. The results are shown in Fig. 15(c) and (d). The common symptoms of AF patient are irregular heart activities and fluttering heartbeat [30]. It can be seen that the extracted DCG waveform is totally disordered. Moreover, the heart rate was hard to find from the spectrum in Fig. 15(d). In this case, the DCG obtained by proposed technique still shared great correlation with ECG. Although the characteristic points A-C can also be positioned on D-DCG waveform according to the positioning method stated above, the ECG waveform lost P wave and T wave made it difficult to verify the accuracy. However, the point B still showed high correspondence with QRS wave.

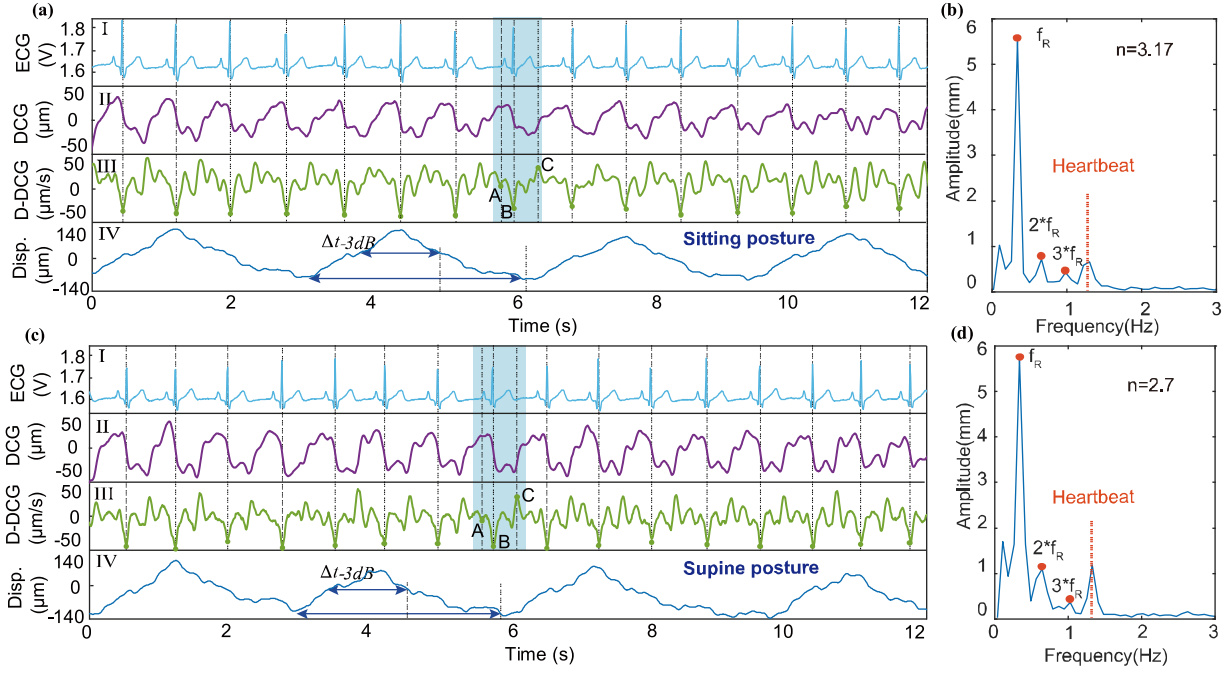


Fig. 14. Experimental results of different DCG measurement conditions: the simultaneously recorded signals of the healthy subject in (a) normal situation with sitting posture, and (c) normal situation with supine posture. (b) and (d) illustrate the spectra of the demodulated displacement of the vital signals for different conditions of (a) and (c), respectively.

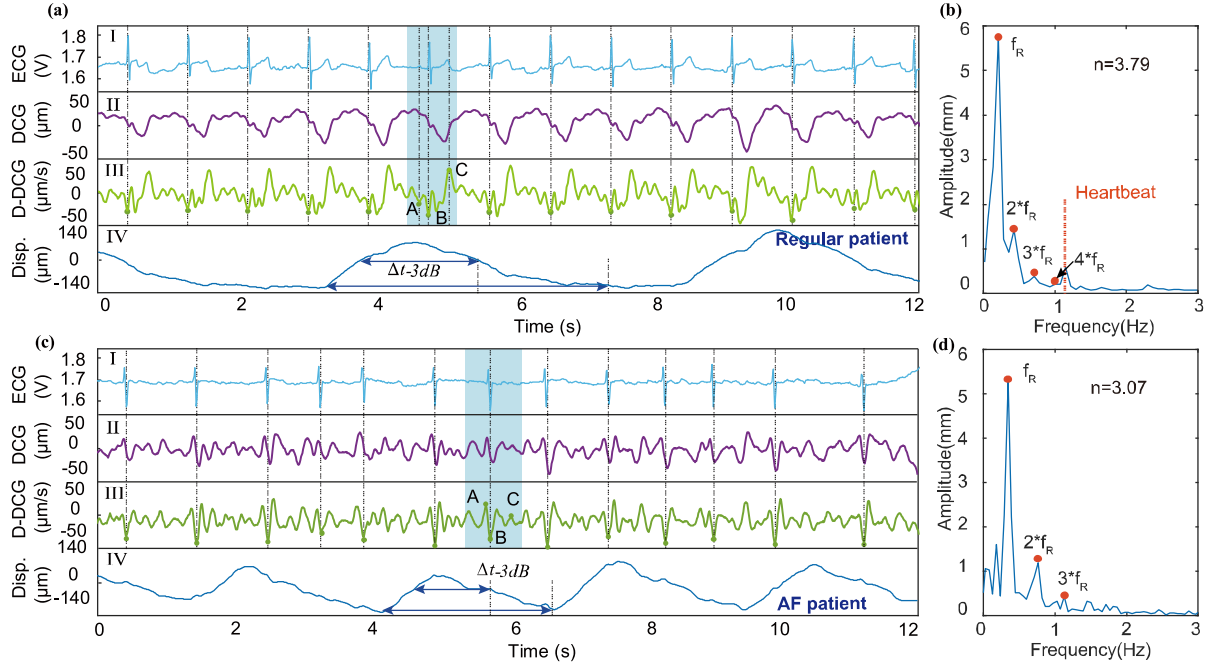


Fig. 15. Experimental results of different patients in clinical environment: the simultaneously recorded signals of (a) regular CHD patient in clinical environment and (c) CHD patient and experienced AF symptoms. (b) and (d) illustrate the spectra of the demodulated displacement of the vital signals for different patients of (a) and (c), respectively.

#### D. R-R Interval Analysis and Diseases Symptoms

In practical applications, HRV has become a reliable index on assessing humans' mental state and physical condition [31], [32], and has been applied to sleep monitoring [31] and stress recognition [32]. In medical application, the accurate HRV analysis requires the R-R intervals measured by ECG [24]. To assess the accuracy of the detected DCGs, the comparisons of R-R intervals retrieved from ECGs and

DCGs from experimental results was made in Fig. 16. The calculated root mean square error (RMSE) and the normalized RMSE (NRMSE) of R-R intervals in the four experiments are 5.5 ms/0.69%, 6.7 ms/0.88%, 10.84 ms/1.27%, and 36.5 ms/3.86%, respectively. Except for the data of AF patient, the other results showed higher accuracy than that of the hold-breath measurement (14.67 ms/1.9% in [11] and 14.51 ms/1.67% in [12]). The increased error of AF patient

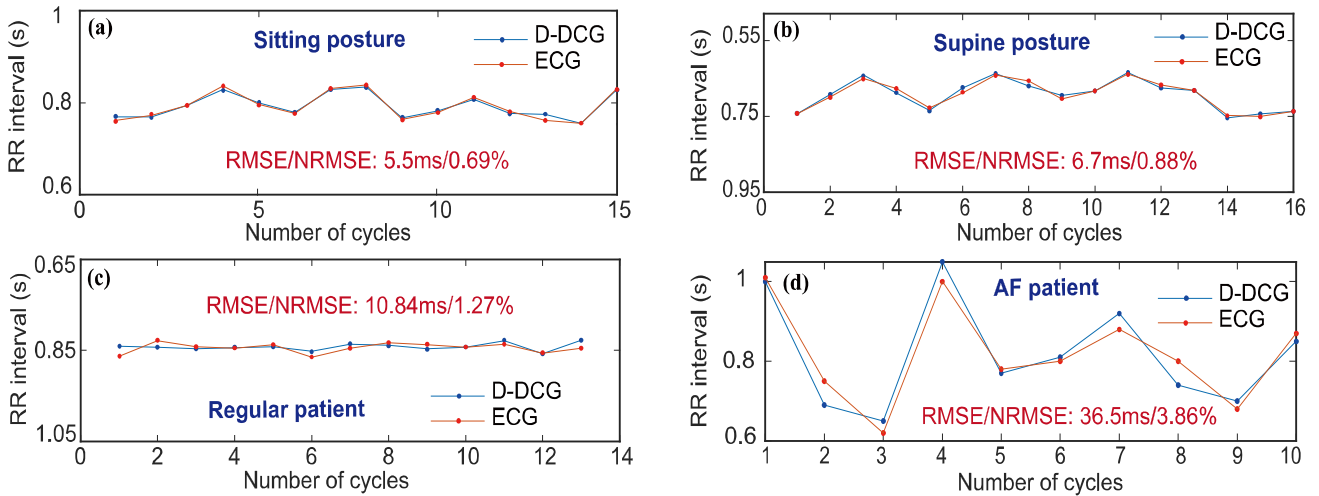


Fig. 16. Comparison of RR intervals retrieved from ECG and D-DCG in the different situation. (a) Healthy subject in normal situation with sitting posture, (b) healthy subject in normal situation with supine posture, (c) regular CHD patient in clinical environment, and (d) CHD patient and experienced AF symptoms in clinical environment.

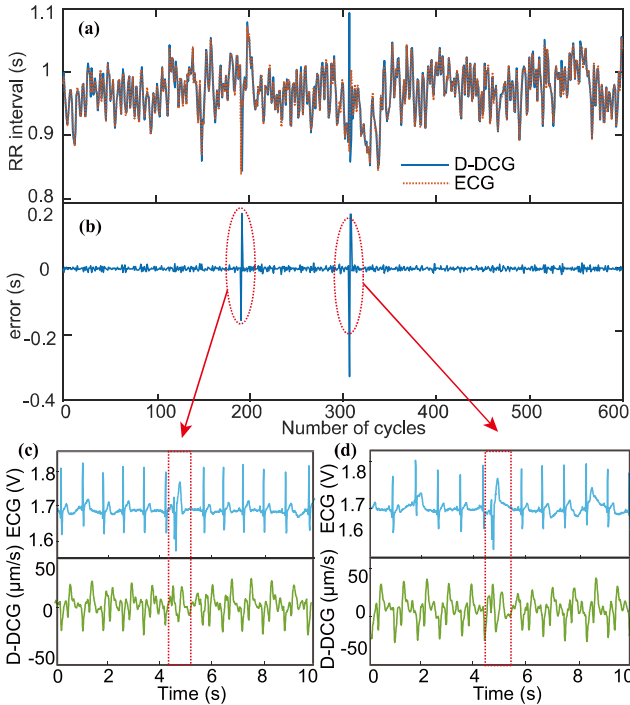


Fig. 17. (a) Comparison between the RR intervals retrieved from the detected ECG and DCGs for long-term monitoring. (b) The RR intervals error estimated by D-DCG waveform with respect to ECG. (c) and (d) are detailed ECG and D-DCG waveforms at the cycles when the error suddenly increased.

might be due to the much weaker activity of the AF than normal cardiac activity. Therefore, it might require more sensitive DRS with shorter wavelength such as the DRS reported in [12].

Then, the long-term experiment was carried out in normal and clinical environments. For the diagnosis of occasional arrhythmia like temporary AF and episodic PHBs, the long-term monitoring is highly required.

First, 10-min DCG detection was conducted of a subject with PHBs under the normal setting of Fig. 13(b). In this condition, the subject was nearly falling asleep. The 10-min R-R interval result and error analysis are shown in

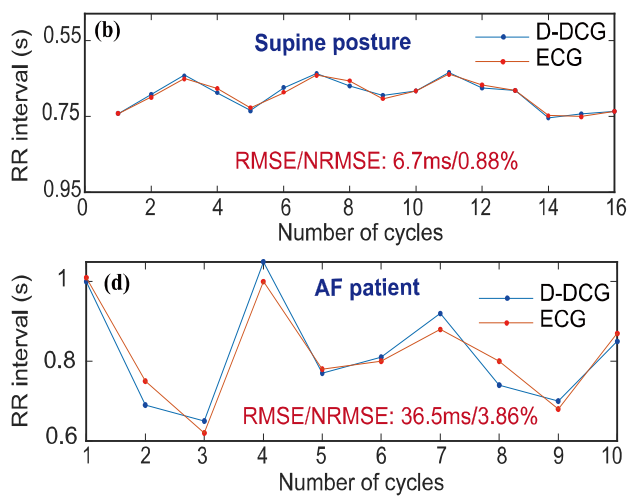
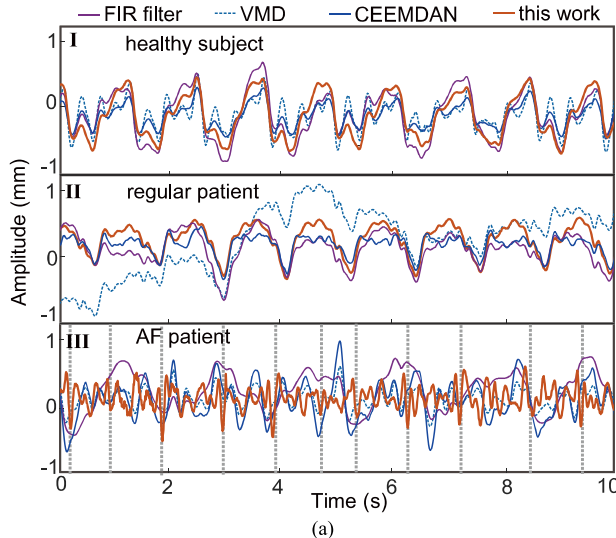


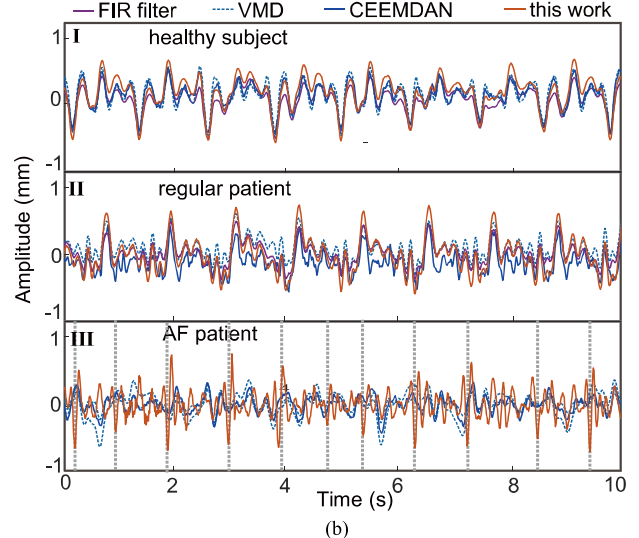
Fig. 18. RR Lorenz plots based on the extracted DCGs in clinical experiments: (a) healthy subject and (b) AF patient.

Fig. 17(a) and (b), respectively. There are two moments when the RR intervals measurement error suddenly increased. From the detailed ECG waveform at these moments, as shown in Fig. 17(c) and (d), it is seen that the subject had occasional PHBs at that time. Moreover, both the ECG and D-DCG waveform were turbulent at these moments which brings great error in the estimation of R-R intervals. It is noted that the positioning of ECGs' R peak and D-DCGs' point B was automatically achieved by Findpeaks function in MATLAB. Thus, the positions of R peak and the point B found by code at PHB occurring moments were both wrong and brings great error compared to other normal segments. The RMSE and NRMSE of R-R intervals are 17.8 ms/1.86%. After removing singular values of error curve in Fig. 17(b), the calculated RMSE and NRMSE are 5.2 ms/0.54%.

Moreover, DCG signals were detected in clinical environment. Since there was a time limit for the patients' postoperative observation, data were collected for a maximum of three minutes in each trial. The Lorenz-RR interval scatterplots of normal patient and persistent AF patient were plotted in Fig. 18. In clinical application, the Lorenz plot plays a significant role in rapid diagnosis of arrhythmia based on Holter analysis. It provides a visual representation of the R-R intervals [33]. Different heart diseases have different patterns. It is seen that the outline of whole scatters of normal patient is fusiform in Fig. 18(a), corresponding to the normal pattern in diagnostic results of Holter. And the outline of whole



(a)



(b)

Fig. 19. Comparison of different DCGs extraction performance: (a) DCG results and (b) D-DCG results. The gray dash lines in Panel III indicate the R waves of ECG.

scatters of persistent AF patient is fan-shaped in Fig. 18(b), corresponding to the AF pattern in diagnostic results of Holter. In addition, due to the irregular heartbeat, the scatters fall into a larger area than normal people. Such significant difference information remotely obtained from DCG detection can be potentially used in heart diseases diagnosis.

It should be noted that during these experiments, the subjects and patients were in stable condition and breathed normally which means the breath frequency is easy to estimate in frequency domain for PRF algorithm. If in the cases that people might breathe irregularly, there can be a signal segmentation part before the PRF algorithm processing to ensure the analyzed signal has steady breathing characteristic.

#### E. Algorithm Performance Comparison

The comparison of the performance of different DCG extraction algorithm in the practical application is shown in Fig. 19. The original signals are from the above experimental data of healthy subject, regular patient, and AF patient. The extracted DCG and D-DCG waveform are both plotted in Fig. 19(a) and (b), respectively.

It can be seen that in Fig. 19(a), the DCGs extracted by PRF algorithm and CEEMDAN algorithm show better periodicity and waveform consistency in the cases of healthy subject and regular patient. However, in the case of AF patient, only the DCG extracted by the PRF algorithm show timing correspondence with the ECG. And according to the computation efficiency analysis in Fig. 9, the CEEMDAN has too long running time which is not suitable for practical application. In all the cases, the FIR filter method and VMD both show large distortion. This is because the respiration signals of these subjects all have high-order respiratory harmonics falling within the DCG band.

The D-DCG extraction comparison is shown in Fig. 19(b). It is seen that these methods show similar periodicity and waveform consistency in the case of healthy subject. The performance of FIR filter and VMD seems to be improved.

This is because the differential operation eliminates the effects of the respiration harmonic interference [34]. However, for the regular patient, the PRF algorithm show obvious better waveform consistency. And for the AF patient, only the D-DCG extracted by the PRF algorithm show timing correspondence with the ECG. All the other methods totally do not work in such situation. A possible explanation is that the irregular heartbeat leads to the serve spectrum overlapping which greatly influences the performance of mode decomposition algorithm.

#### F. Summary

The experiment part includes simulation experiment and practical experiments in different environments. The simulation experimental result verified the high linearity of the Doppler radar system and ensured that the waveform details of detected DCGs are not caused by hardware nonlinearity which is important for DCG detection.

Sequentially, for the practical experimental results, the accurate measurement results of R-R intervals of subject in different postures and different environments verified the stability of DCG detection with proposed PRF algorithm. Compared to conventional signal separation methods, the proposed PRF algorithm can effectively extract heart motion signals from chest-wall motion mixed with respiratory signal with no need to estimate the heartbeat frequency. Also, compared to simple FIR filter with fixed cutoff frequency, the PRF algorithm showed higher recovery performance.

However, the DCGs detected by the designed K-band Doppler radar system in this work are hard to be used for positioning the characteristic points D, D', E', and E reported in [12] where the DCG was detected by a V-band radar when subject hold his breath. However, the D-DCG waveform shows better correspondence with ECG signal in this work and the measurements of R-R intervals retrieved from D-DCGs of healthy people have higher accuracy than the measurement in previous papers [11], [12]. This is because the

differential operation eliminates the effects of the respiration interference [34].

The accurate measurement of R-R intervals in long-term experiments achieves the reliable HRV analysis based on contactless detection by Doppler radar, which might expand the use of radar in daily health monitoring like sleep monitoring and stress estimation. Moreover, the D-DCG waveforms of patients from those of heart diseases like AF and PHB show significant difference with the normal subjects. And for AF patient, this work provided Lorenz plots of R-R intervals detected by DRS, and the results show similar patterns to the diagnostic results of Holter. These results indicate the proposed method in this work can be used for auxiliary diagnosis of heart diseases in the future.

#### IV. CONCLUSION

In conclusion, a *K*-band 24-GHz dc-coupled CW Doppler radar system was custom-designed and a novel PRF algorithm was proposed to obtain the accurate DCGs in the presence of respiration. Both simulation and experimental results showed the proposed PRF algorithm have best performance compared to conventional methods. Furthermore, the experimental results in normal and clinical environments showed the DRS with proposed algorithm has promising potential in HRV analysis and heart diseases diagnosis which provides a convenient, comfortable and reliable way for daily homecare and clinical application.

#### REFERENCES

- [1] C. Li, V. M. Lubecke, O. Boric-Lubecke, and J. Lin, "A review on recent advances in Doppler radar sensors for noncontact healthcare monitoring," *IEEE Trans. Microw. Theory Techn.*, vol. 61, no. 5, pp. 2046–2060, May 2013.
- [2] D. Stuckler, "Population causes and consequences of leading chronic diseases: A comparative analysis of prevailing explanations," *Milbank Quart.*, vol. 86, no. 2, pp. 273–326, Jun. 2008.
- [3] R. J. Martis, U. R. Acharya, and H. Adeli, "Current methods in electrocardiogram characterization," *Comput. Biol. Med.*, vol. 48, pp. 133–149, May 2014.
- [4] J. Wang, X. Wang, Z. Zhu, J. Huangfu, C. Li, and L. Ran, "1-D microwave imaging of human cardiac motion: An *ab-initio* investigation," *IEEE Trans. Microw. Theory Techn.*, vol. 61, no. 5, pp. 2101–2107, May 2013.
- [5] Y. Zhang, F. Qi, H. Lv, F. Liang, and J. Wang, "Bioradar technology: Recent research and advancements," *IEEE Microw. Mag.*, vol. 20, no. 8, pp. 58–73, Aug. 2019.
- [6] J. C. Lin, J. Kiernicki, M. Kiernicki, and P. B. Wollschlaeger, "Microwave apexcardiography," *IEEE Trans. Microw. Theory Techn.*, vol. 27, no. 6, pp. 618–620, Jun. 1979.
- [7] K. Shi *et al.*, "Automatic signal quality index determination of radar-recorded heart sound signals using ensemble classification," *IEEE Trans. Biomed. Eng.*, vol. 67, no. 3, pp. 773–785, Mar. 2020.
- [8] C.-H. Tseng, T.-J. Tseng, and C.-Z. Wu, "Cuffless blood pressure measurement using a microwave near-field self-injection-locked wrist pulse sensor," *IEEE Trans. Microw. Theory Techn.*, vol. 68, no. 11, pp. 4865–4874, Nov. 2020.
- [9] Y. Yuan and C.-T.-M. Wu, "Non-contact fingertip microwave plethysmography based on near-field sensing with super-regenerative oscillator," in *IEEE MTT-S Int. Microw. Symp. Dig.*, Jun. 2021, pp. 362–365.
- [10] W. Xia, Y. Li, and S. Dong, "Radar-based high-accuracy cardiac activity sensing," *IEEE Trans. Instrum. Meas.*, vol. 70, pp. 1–13, 2021.
- [11] S. Dong *et al.*, "Doppler cardiogram: A remote detection of human heart activities," *IEEE Trans. Microw. Theory Techn.*, vol. 68, no. 3, pp. 1132–1141, Mar. 2020.
- [12] C. Zhu *et al.*, "Doppler cardiogram detected by a V-band Doppler radar sensor," *IEEE Trans. Microw. Theory Techn.*, vol. 70, no. 1, pp. 521–531, Jan. 2022.
- [13] C. Gu *et al.*, "Accurate respiration measurement using DC-coupled continuous-wave radar sensor for motion-adaptive cancer radiotherapy," *IEEE Trans. Biomed. Eng.*, vol. 59, no. 11, pp. 3117–3123, Nov. 2012.
- [14] D. R. Morgan and M. G. Zierdt, "Novel signal processing techniques for Doppler radar cardiopulmonary sensing," *Signal Process.*, vol. 89, no. 1, pp. 45–66, Jan. 2009.
- [15] C. Li, J. Ling, J. Li, and J. Lin, "Accurate Doppler radar noncontact vital sign detection using the RELAX algorithm," *IEEE Trans. Instrum. Meas.*, vol. 59, no. 3, pp. 687–695, Mar. 2010.
- [16] Y. Xiong, S. Chen, X. Dong, Z. Peng, and W. Zhang, "Accurate measurement in Doppler radar vital sign detection based on parameterized demodulation," *IEEE Trans. Microw. Theory Techn.*, vol. 65, no. 11, pp. 4483–4492, Nov. 2017.
- [17] F.-K. Wang, P.-H. Juan, D.-M. Chian, and C.-K. Wen, "Multiple range and vital sign detection based on single-conversion self-injection-locked hybrid mode radar with a novel frequency estimation algorithm," *IEEE Trans. Microw. Theory Techn.*, vol. 68, no. 5, pp. 1908–1920, May 2020.
- [18] M. Li and J. Lin, "Wavelet-transform-based data-length-variation technique for fast heart rate detection using 5.8-GHz CW Doppler radar," *IEEE Trans. Microw. Theory Techn.*, vol. 66, no. 1, pp. 568–576, Jan. 2018.
- [19] Q. Lv *et al.*, "Doppler vital signs detection in the presence of large-scale random body movements," *IEEE Trans. Microw. Theory Techn.*, vol. 66, no. 9, pp. 4261–4270, Sep. 2018.
- [20] S. Dong, C. Gu, L. Ran, and J.-F. Mao, "Doppler cardiogram detection in the presence of respiration with a K-band radar sensor," in *Proc. IEEE Radio Wireless Symp. (RWS)*, Jan. 2022, pp. 45–48.
- [21] T. Zheng, Z. Chen, C. Cai, J. Luo, and X. Zhang, "V2iFi: In-vehicle vital sign monitoring via compact RF sensing," *Proc. ACM Interact., Mobile, Wearable Ubiquitous Technol.*, vol. 4, no. 2, pp. 1–27, 2020.
- [22] M. E. Torres, M. A. Colominas, G. Schlotthauer, and P. Flandrin, "A complete ensemble empirical mode decomposition with adaptive noise," in *Proc. IEEE Int. Conf. Acoust., Speech Signal Process. (ICASSP)*, May 2011, pp. 4144–4147.
- [23] F. Gustafsson, "Determining the initial states in forward-backward filtering," *IEEE Trans. Signal Process.*, vol. 44, no. 4, pp. 988–992, Apr. 1996.
- [24] B. Xhyheri, O. Manfrini, M. Mazzolini, C. Pizzi, and R. Bugiardini, "Heart rate variability today," *Prog. Cardiovascular Diseases*, vol. 55, no. 3, pp. 321–331, 2012.
- [25] W. Xu, Y. Li, C. Gu, and J.-F. Mao, "Large displacement motion interferometry with modified differentiate and cross-multiply technique," *IEEE Trans. Microw. Theory Techn.*, vol. 69, no. 11, pp. 4879–4890, Nov. 2021.
- [26] L. E. Teichholz, "Problems in echocardiographic volume determinations: Echocardiographic-angiographic correlations in the presence or absence of asynchrony," *Amer. J. Cardiol.*, vol. 37, no. 1, pp. 7–11, Jan. 1976.
- [27] P. Dehkordi *et al.*, "Comparison of different methods for estimating cardiac timings: A comprehensive multimodal echocardiography investigation," *Frontiers Physiol.*, vol. 10, p. 1057, Aug. 2019.
- [28] S. Schellenberger *et al.*, "A dataset of clinically recorded radar vital signs with synchronised reference sensor signals," *Sci. Data*, vol. 7, no. 1, pp. 1–11, Dec. 2020.
- [29] K. Al-Jabery, T. Obafemi-Ajaya, G. Olbricht, and D. Wunsch, *Computational learning approaches to data analytics in Biomedical Applications*. New York, NY, USA: Academic, 2019.
- [30] A. S. Go *et al.*, "Prevalence of diagnosed atrial fibrillation in adults: National implications for rhythm management and stroke prevention: The anticoagulation and risk factors in atrial fibrillation (ATRIA) study," *Jama*, vol. 285, no. 18, pp. 2370–2375, 2001.
- [31] I. Grittì, S. Defendi, C. Mauri, G. Banfi, P. Duca, and G. S. Roi, "Heart rate variability, standard of measurement, physiological interpretation and clinical use in mountain Marathon runners during sleep and after acclimatization at 3480 m," *J. Behav. Brain Sci.*, vol. 3, no. 1, pp. 26–48, 2013.
- [32] J. F. Thayer *et al.*, "A meta-analysis of heart rate variability and neuroimaging studies: Implications for heart rate variability as a marker of stress and health," *Neurosci. Biobehav. Rev.*, vol. 36, no. 2, pp. 747–756, 2012.
- [33] H. D. Esperer, C. Esperer, and R. J. Cohen, "Cardiac arrhythmias imprint specific signatures on Lorenz plots," *Ann. Noninvasive Electrocardiol.*, vol. 13, no. 1, pp. 44–60, Jan. 2008.
- [34] Y. Xiong, Z. Peng, C. Gu, S. Li, D. Wang, and W. Zhang, "Differential enhancement method for robust and accurate heart rate monitoring via microwave vital sign sensing," *IEEE Trans. Instrum. Meas.*, vol. 69, no. 9, pp. 7108–7118, Sep. 2020.



**Shuqin Dong** (Graduate Student Member, IEEE) received the B.S. degree in electronic and information engineering from Xidian University, Xi'an, China, in 2017, and the M.S. degree in electronic science and technology from Zhejiang University, Hangzhou, China, in 2020. She is currently pursuing the Ph.D. degree in electronic and information at Shanghai Jiao Tong University, Shanghai, China.

From 2020 to 2021, she was a Software Algorithm Engineer with Huawei, Guangdong, China. Her research interests include biomedical radar, health informatics, and signal processing.



**Yuchen Li** (Graduate Student Member, IEEE) received the B.S. degree in electromagnetic field and wireless technology from the University of Electronic Science and Technology of China, Chengdu, China, in 2020. He is currently pursuing the Ph.D. degree in electrical engineering at Shanghai Jiao Tong University, Shanghai, China.

His current research interests include short-range radar sensor and sensing systems, new concept human-computer interaction (HCI), radar-based gesture sensing, and wireless sensing and its various applications in AI/AR/IoT.



**Jingyun Lu** (Graduate Student Member, IEEE) received the B.S. degree from the Huazhong University of Science and Technology, Wuhan, China, in 2019, and the M.S. degree from Shanghai Jiao Tong University, Shanghai, China, in 2022, where he is currently pursuing the Ph.D. degree.

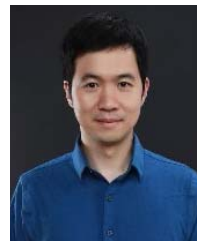
His current research interests include microwave/millimeter-wave integrated circuits, full-duplex systems, and biomedical applications of wireless sensing.



**Zhi Zhang** received the B.S. degree in clinical medicine from Nanjing Medical University, Nanjing, China, in 2001, the M.S. degree in cardiology from the Medical School, Fudan University, Shanghai, China, in 2005, and the Ph.D. degree in cardiology from the Medical School, Shanghai Jiao Tong University, Shanghai, in 2011.

He was a Post-Doctoral Fellow with Wake Forest University, Winston-Salem, NC, USA, in 2016. He is currently the Deputy Director of Hypertension Department at the First Affiliated People's Hospital affiliated to Shanghai Jiao Tong University and a Training Tutor with the National Health Commission Coronary Heart Disease Intervention. He is also an Associate Physician with the Department of Cardiology, First People's Hospital affiliated to Shanghai Jiao Tong University. He is a Master Supervisor of the Shanghai Jiao Tong University School of Medicine, and a Master Supervisor and an Associate Professor at Nanjing Medical University.

Dr. Zhang is also a Fellow of the Interventional Branch of Shanghai Association of Traditional Chinese Medicine.



**Changzhan Gu** (Senior Member, IEEE) received the B.S. and M.S. degrees from Zhejiang University, Hangzhou, China, in 2006 and 2008, respectively, the M.S. degree from the University of Florida, Gainesville, FL, USA, in 2010, and the Ph.D. degree in electrical engineering from Texas Tech University, Lubbock, TX, USA, in 2013.

Before returning to academia, he was with Google, Mountain View, CA, USA, where he was involved in the research and development of millimeter-wave gesture radar technology and translating it into consumer products. He is currently an Associate Professor with Shanghai Jiao Tong University, Shanghai, China.

Dr. Gu is a member of the IEEE MTT-S TC28 and a Secretary of MTT-S Shanghai Chapter. He is the TPC Chair of the 2022 IEEE International Microwave Biomedical Conference (IMBioC). He received the Best/Excellent Paper Awards (eight times) from IEEE conferences as an author/coauthor. He received the IEEE Sensors Council Early Career Technical Achievement Award in 2019, the Okawa Foundation Research Grant in 2019, and the IEEE MTT-S Graduate Fellowship in Medical Applications in 2013. He was an Associate Editor of the IEEE TRANSACTIONS ON BIOMEDICAL CIRCUITS AND SYSTEMS (TBioCAS) (2019–2021) and a Guest Editor of the IEEE TRANSACTIONS ON MICROWAVE THEORY AND TECHNIQUES SPECIAL ISSUE on RWW2022. He is an Associate Editor of the IEEE JOURNAL OF ELECTROMAGNETICS, RF and Microwaves in Medicine and Biology (J-ERM) and the IET Microwaves, Antennas & Propagation (MAP).



**Junfa Mao** (Fellow, IEEE) received the B.S. degree in radiation physics from the National University of Defense Technology, Changsha, China, in 1985, the M.S. degree in experimental nuclear physics from the Shanghai Institute of Nuclear Research, Chinese Academy of Sciences, Beijing, China, in 1988, and the Ph.D. degree in electronic engineering from Shanghai Jiao Tong University, Shanghai, China, in 1992.

Since 1992, he has been a Faculty Member of Shanghai Jiao Tong University, where he is currently a Chair Professor and the Vice President. He has authored or coauthored more than 500 articles (including more than 150 IEEE journal articles). His research interests include interconnect and package problem of integrated circuits and systems and the analysis and design of microwave components and circuits.

Dr. Mao is an academician of the Chinese Academy of Science. He was a member of the 2012–2014 IEEE Microwave Theory and Techniques Society Fellow Evaluation Committee and the 2015 IEEE Fellow Committee, and the Founder and the 2007–2009 Chair of the IEEE Shanghai Section. He is a Fellow of CIE. He received the National Natural Science Award of China in 2004, the National Technology Invention Award of China in 2008, the National Science and Technology Advancement Award of China in 2012, ten best paper awards of international conferences, and two National Awards of Teaching in 2005 and 2018. He is a Chief Scientist of the National Basic Research Program (973 Program) of China, the Project Leader of the Natural Science Foundation of China for Creative Research Groups, a Cheung Kong Scholar of the Ministry of Education, China, the Director of the Microwave Society of China Institute of Electronics (CIE), and the 2009–2019 Chair of the IEEE MTT-S Shanghai Chapter.